

A displaced lower mantle source of the Hainan plume in South China revealed by receiver function imaging of the CEArray

Yan Zhang¹, Fenglin Niu², Jieyuan Ning³, and Chunquan Yu¹

¹Southern University of Science and Technology

²Rice University

³Peking University

September 30, 2023

Abstract

We analyzed 49,592 teleseismic receiver functions recorded by 278 CEArray stations to image the mantle transition zone (MTZ) beneath the South China Block to understand origins of deep velocity anomalies and their potential links to subduction and intraplate volcanism. We employed a fast-marching method and a high-resolution 3-D velocity model (FWEA18) derived from full waveform inversion in computing P-to-S conversion times to better image the 410-km and 660-km discontinuities. Our results indicate that the common-conversion-point stacking of receiver functions using 3-D conversion times yielded better migration images of the two discontinuities. The images revealed a slightly depressed 410-km with a few small uplifted patches, and showed that the 660-km beneath the western Yangtze Craton is depressed by 10-25 km, which is likely caused by the stagnant Paleo-Pacific slab. The 660-km beneath the southern Cathaysia Block has a 5-15 km high plateau with a topographic low at its central part. The lateral dimension of the topographic low is ~150 km and located beneath the central Pearl River Mount Basin near Hong Kong. We speculate the topographic low occurs within the Hainan plume with a temperature excess of ~300-400 K and is caused by the garnet phase transition. The displaced deep plume enters the MTZ and spreads nearly horizontally at the base. The plume evolves into two channels with a minor one toward the northeast and a major one toward the southwest, which keep moving upward to the 410-km. The southwest channel is likely the source that feeds the Hainan volcanoes.

Hosted file

974603_0_art_file_11409915_s1c4wx.docx available at <https://authorea.com/users/667905/articles/667936-a-displaced-lower-mantle-source-of-the-hainan-plume-in-south-china-revealed-by-receiver-function-imaging-of-the-cearray>

Hosted file

974603_0_supp_11410050_s1c5vh.docx available at <https://authorea.com/users/667905/articles/667936-a-displaced-lower-mantle-source-of-the-hainan-plume-in-south-china-revealed-by-receiver-function-imaging-of-the-cearray>

1 **A displaced lower mantle source of the Hainan plume in South China revealed by receiver**
2 **function imaging of the CEArray**

3 Yan Zhang¹, Fenglin Niu^{2,3}, Jieyuan Ning^{4,*} and Chunquan Yu¹

4 ¹*Department of Earth and Space Sciences, Southern University of Science and Technology, Shenzhen, China*

5 ²*Department of Earth, Environmental and Planetary Sciences, Rice University, Houston, Texas, USA*

6 ³*State Key Laboratory of Petroleum Resources and Engineering and Unconventional Petroleum Research*
7 *Institute, China University of Petroleum at Beijing, Beijing, China*

8 ⁴*Institute of Theoretical and Applied Geophysics, Peking University, Beijing, China*

9 *Corresponding author: Jieyuan Ning, njy@pku.edu.cn

10

11 **Key Points:**

- 12 • *FWEA18* is used in migrating CEArray RFs to image the MTZ beneath the South China Block.
13 • The 660-km is depressed ~10-25 km by stagnant slabs beneath the northwestern part of the block.
14 • The Hainan volcanoes are fed by a displaced lower mantle plume beneath the central Pearl River
15 Mouth Basin.

16

17 **Abstract**

18 We analyzed 49,592 teleseismic receiver functions recorded by 278 CEArray stations to image the mantle
19 transition zone (MTZ) beneath the South China Block to understand origins of deep velocity anomalies and their
20 potential links to subduction and intraplate volcanism. We employed a fast-marching method and a high-
21 resolution 3-D velocity model (*FWEA18*) derived from full waveform inversion in computing P-to-S conversion
22 times to better image the 410-km and 660-km discontinuities. Our results indicate that the common-conversion-
23 point stacking of receiver functions using 3-D conversion times yielded better migration images of the two
24 discontinuities. The images revealed a slightly depressed 410-km with a few small uplifted patches, and showed
25 that the 660-km beneath the western Yangtze Craton is depressed by 10-25 km, which is likely caused by the
26 stagnant Paleo-Pacific slab. The 660-km beneath the southern Cathaysia Block has a 5-15 km high plateau with
27 a topographic low at its central part. The lateral dimension of the topographic low is ~150 km and located beneath
28 the central Pearl River Mount Basin near Hong Kong. We speculate the topographic low occurs within the Hainan
29 plume with a temperature excess of ~300-400 K and is caused by the garnet phase transition. The displaced deep
30 plume enters the MTZ and spreads nearly horizontally at the base. The plume evolves into two channels with a
31 minor one toward the northeast and a major one toward the southwest, which keep moving upward to the 410-
32 km. The southwest channel is likely the source that feeds the Hainan volcanoes.

33 **Plain Language Summary**

34 Using data from seismic stations in the South China Block, we investigated the mantle transition zone to
35 understand the origins of deep velocity anomalies and their associations with subduction and intraplate
36 volcanism. By applying advanced techniques and a ground-truth reference model, we obtained clearer images
37 of the 410-km and 660-km discontinuities. The images showed that the 410-km discontinuity is slightly
38 depressed with some small uplifted areas. Additionally, the 660-km discontinuity beneath the western Yangtze
39 Craton is depressed due to the presence of a stagnant slab from the ancient Pacific Ocean. In contrast, beneath
40 the southern Cathaysia Block, the 660-km discontinuity forms a high plateau with a central low area. This area
41 located near Hong Kong, may be related to a plume originating from the lower mantle. The plume, with elevated
42 temperatures, enters the mantle transition zone and spreads horizontally. It then evolves into two channels, with
43 one moving towards the northeast and the other towards the southwest. The southwest channel likely supplies
44 magma to the volcanoes in Hainan. These findings provide insights into the complex processes occurring deep
45 within the Earth's mantle in the South China region.

46

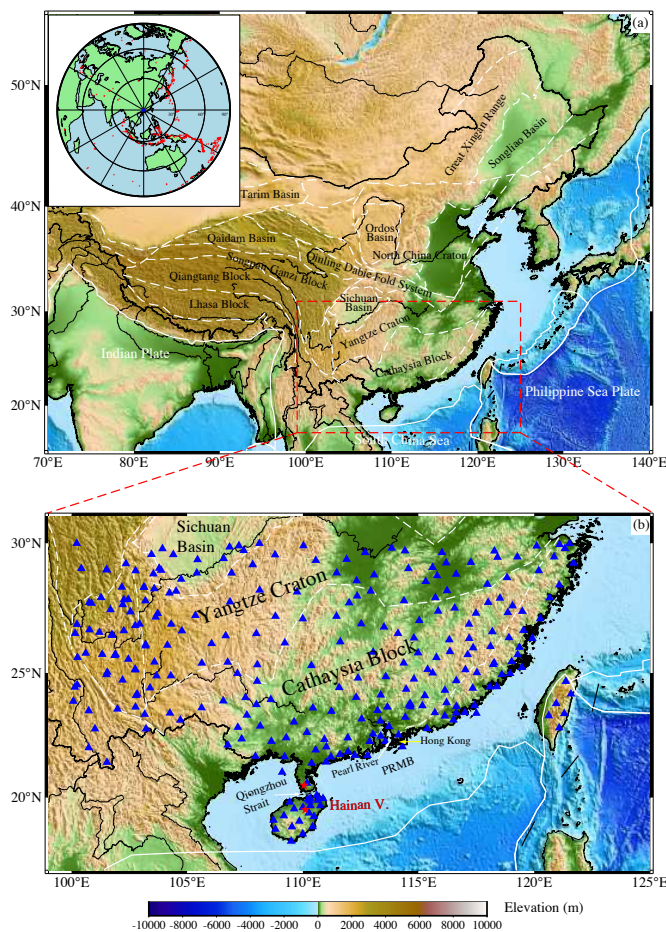
47 1. Introduction

48 The South China Block (SCB) was formed during the Neoproterozoic when the Yangtze Craton in the
49 northwest and the Cathaysia Block in the southwest amalgamated along the Jiangnan orogenic belt (e.g., Zhao,
50 2015). SCB is situated on the southeastern part of the Eurasian plate and has experienced a long history of
51 deformation and magmatism associated with subduction of oceanic plates, collision of continental plates and
52 upwelling of mantle plume (Briais et al., 1993; Zheng & Zhang, 2007). Tomographic investigations have
53 unveiled significant high- and low-velocity anomalies inside the mantle transition zone (MTZ) under the SCB
54 (e.g., Huang & Zhao, 2006; Li & Van der Hilst, 2010; Zhou et al., 2012). While the high-velocity anomalies are
55 usually referred to the subducted slabs of oceanic plates or delaminated continental lithosphere, the low-velocity
56 anomalies have been attributed to the Hainan plume arising from the lower mantle (e.g., Huang, 2014; Xia et al.,
57 2016; Tao et al., 2018). The exact location of the Hainan plume in the lower mantle is, however, not well resolved
58 partially because traveltimes tomography intrinsically has poor resolution on deep low-velocity structures. In
59 addition, the sensitivity of seismic velocity to temperature becomes weak in the lower mantle (e.g., Trampert et
60 al., 2001), making it harder to image temperature anomalies in the lower mantle.

61 The MTZ is located between the upper mantle and lower mantle and is marked by sharp increases in seismic
62 velocity and density in the top and bottom of the zone, which are known as the 410-km and 660-km seismic
63 discontinuities (hereafter referred to as 410-km and 660-km). The two seismic discontinuities occurred at depths
64 where mantle minerals undergo phase changes in crystal structure observed by experiment studies (e.g., Katsura
65 & Ito, 1989). The 410-km is associated with a phase transition of olivine to wadsleyite at a pressure of ~14 GPa,
66 while the 660-km corresponds to the transition from ringwoodite to perovskite (also known as bridgmanite) and
67 ferropericlase at a pressure of ~24 GPa (e.g., Ita & Stixrude, 1992). Experimental studies (e.g., Katsura & Ito,
68 1989; Ita & Stixrude, 1992) showed that the 410-km phase transition is an exothermic reaction with a positive
69 Clapeyron slope and the 660-km one is an endothermic reaction with a negative Clapeyron slope; a decrease in
70 temperature (i.e., cold slab) results in a shallower 410-km and a deeper 660-km, leading to a thicker MTZ, while
71 an excess of mantle temperature (i.e., hot plume) results in a thinner MTZ owing to a depressed 410-km and an
72 uplifted 660-km. In summary, the depths of the 410-km and 660-km in different tectonic settings are expected
73 to vary with mantle temperature, and thus their depths can be used as thermometers to make in-situ measurements
74 of temperature inside the MTZ. Therefore, mapping lateral variations of the 410-km and 660-km can provide
75 information complementary to velocity structures in constraining temperature anomalies around the MTZ.

76 Receiver functions (RFs) have been widely used in imaging the 410-km and 660-km beneath a seismic array.
77 In the SCB, many studies using RF data recorded by arrays with various size and density have been conducted
78 (e.g., Ai et al., 2007; Huang et al., 2014; Huang et al., 2015; Wei & Chen, 2016; Han et al., 2020; He & Santosh,
79 2021) to investigate the MTZ beneath different parts of the SCB. These studies have found significant lateral
80 variations in the depth of the two discontinuities and some correlations between the observed depth structures

81 and velocity anomalies in tomographic models. However, we noticed that several of these studies used 1-D
 82 reference models (e.g., Ai et al., 2007) in computing the traveltime moveouts of the P-to-S conversions at the
 83 two discontinuities, therefore the estimated depths of the 410-km and 660-km could be significantly biased by
 84 unmodeled 3-D velocity structures. Due to the lack of P- and S-wave velocity models with comparable accuracy
 85 and resolution, the other studies (e.g., Huang et al., 2015) used either a 3-D P- or S-wave velocity model and a
 86 constant scaling relationship of $\delta \ln V_s / \delta \ln V_p$ to compute the P-to-S conversion times, which could also introduce
 87 some artifacts to RF images. Therefore, there are large discrepancies in the estimated depths of the two
 88 discontinuities, as well as the MTZ thickness among these studies, which could be caused by differences in data
 89 coverage and reference velocity models. Consequently, questions like where the Hainan plume emerges from
 90 the lower mantle and what trajectory it takes in the MTZ are yet to be answered by RF images.



91
 92 **Figure 1.** (a) Topographic map showing the Southeast Asia and the South China Block. The white solid and dashed lines denote
 93 the boundaries of plates and active tectonic blocks, respectively. The rectangle outlined by the red dashed lines represents the study
 94 area that includes the Cathaysia Block, the Yangtze Block and part of the southeastern margin of the Tibetan plateau. Inset in the
 95 upper left corner is an azimuthal equidistant map showing the 623 earthquakes (red stars) used in computing RFs. The blue triangle
 96 in the center indicates the center of the study area, and three circles denote the epicentral distances of 30°, 60°, and 90°, respectively.

97 (b) Distribution of the 278 stations used in the study (blue triangles). The red stars denote the Hainan volcanoes. PRMB: Pearl
98 River Mouth Basin.

99 In this study, we utilized a high-resolution ground truth 3-D P- and S-wave velocity model, *FWEA18* (Tao
100 et al., 2018), which was derived from full waveform inversion of both body wave and surface wave data, as the
101 reference velocity model and the fast marching method (FMM) in numerically solving the 3-D eikonal equation
102 (Kool et al., 2006; Rawlinson & Sambridge, 2004a, 2004b; Guan & Niu, 2018) to compute accurate relative
103 traveltimes of P-to-S converted waves with respect to the direct P arrivals. We compiled 49,592 high-quality RFs
104 recorded by 278 broadband seismic stations that provide a good coverage of the SGB (Figure 1b). We also
105 employed a common-conversion-point (CCP) stacking technique to perform the depth migration of the RFs. The
106 P-to-S conversion events at the 410-km and 660-km are clearly shown in the CCP images. We compared lateral
107 variations of the discontinuity depths with velocity anomalies of the *FWEA18* model, which provide valuable
108 insights into the deep geodynamic processes in the SCB region, especially regarding the deep origin of the
109 Hainan plume as well its kinematics in the MTZ and upper mantle.

110 2. Data and Methods

111 2.1. CEArray data

112 The waveform data used in this study are recorded by the permanent broadband seismic network operated
113 by the China Earthquake Administration (CEA), which is hereafter referred to as the CEArray. The CEArray
114 consists of a backbone national seismograph network (CNDSN), 31 regional networks, and several small
115 aperture arrays with more than 1000 stations (Zheng et al., 2009). We selected 261 CEArray stations located in
116 a rectangular area between 100°-122°E and 18°-30°N, which includes the SCB and its surrounding areas (Figure
117 1b). We also included 17 temporal stations in the southeastern margin of the Tibetan Plateau (SE Tibet) to ensure
118 a relatively even distribution of the broadband stations. We examined waveforms from 623 earthquakes, each
119 with a magnitude greater than 5.0 and an epicentral distance ranging from 30° to 90° (Figure 1a inset), which
120 are recorded by the CEArray stations between 08/2007 and 07/2010 and the temporary stations between 09/2003
121 and 09/2004. These earthquakes offer good coverage in terms of both distance and azimuth (Figures S1a and
122 S1b).

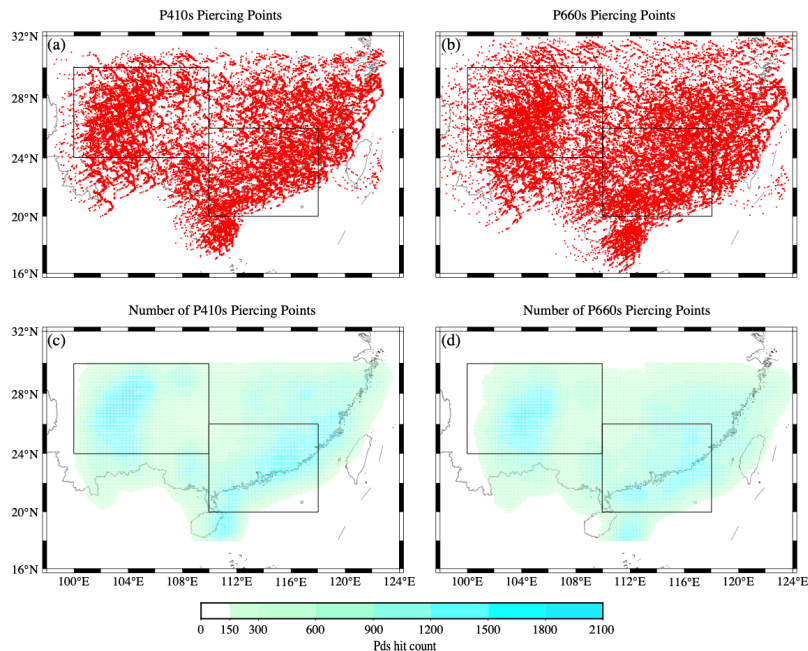
123 2.2. Receiver functions

124 We followed Liu et al. (2015) to compute RFs from teleseismic data and performed CCP stacking to image
125 the 410-km and 660-km. We first used the method of Niu and Li (2011) to estimate true orientations of the two
126 horizontal components for each station using the collected teleseismic data, and then applied a correction if a
127 station showed a misalignment of greater than 5°. The north (N) and east (E) components were then rotated to
128 the radial (R) and transverse (T) directions. We applied a bandpass filtered to the R-T-Z with a corner frequency
129 of 0.01-5 Hz and down-sampled the data to 20 samples per second (sps). We applied the “water-level”

130 deconvolution technique (Clayton & Wiggins, 1976) to the R and Z records to generate RFs. The water level
 131 was set to 0.01 and the Gaussian lowpass filter parameter was set to 1.5, equivalent to a corner frequency of ~0.5
 132 Hz. We manually examined all the RFs and selected a total of 49,592 RFs with a high signal-to-noise ratio (SNR)
 133 for CCP stacking. The P-to-S converted waves at the 410-km (P410s) and the 660-km (P660s) are clearly
 134 observed around the expected arrival times (Figure S1c), indicating sharp velocity contrasts at the two depths.

135 2.3. 3-D *Pds* traveltimes

136 We applied CCP stacking based migration technique to enhance P-to-S conversions that share a common
 137 geographic location. Here we first computed the raypaths of a P-to-S conversion at a depth, d , below the seismic
 138 station, Pds , by raytracing the 1D *IASP91* model (Kennett & Engdahl, 1991). Figures 2a and 2b show the
 139 geographic distributions of the P410s and P660s, which suggest that the study area is well sampled by the RF
 140 dataset. Seismic migration is the process of back projecting signals recorded on seismograms in time domain to
 141 their subsurface source structures in the depth domain. To perform the time-to-depth conversion, the relative
 142 traveltimes of Pds with respect to the direct P arrival needs to be computed through a reference model. As the Pds
 143 traveltimes are affected by conversion depth and V_p and V_s structure above the conversion, an accurate 3-D
 144 reference model is crucial for the depth migration. Conventionally, the relative Pds traveltimes are first computed
 145 through a 1-D average model, such as the *IASP91* model, and then a 3-D traveltimes correction is computed by
 146 integrating anomalies along the 1-D raypath of Pds using the 3-D reference model (Liu et al., 2015). This
 147 raytracing approach is very time-consuming when tens of thousands of RFs are used. In addition, the 1-D raypath
 148 also can introduce significant errors in Pds traveltimes when prominent 3-D velocity anomalies are present in the
 149 upper mantle.



151 **Figure 2.** Lateral distribution of the P410s (a) and P660s (b) piercing points are shown in red dots. Distribution of the P410s hit
152 count (c) and P660s hit count (d). The black rectangles indicate the representative areas of the Yangtze Craton and Cathaysia Block,
153 respectively, for statistical analyses of the depths of the 410-km and 660-km.

154 We adopted the technique developed by Guan and Niu (2018) to calculate the 3-D *Pds* traveltimes with the
155 3-D *FWEA18* model using the numerical eikonal solver, FMM (Kool et al., 2006). Here we briefly review the
156 three steps in computing *Pds* traveltime for each RF: (1) For each earthquake, we define a 3-D volume (hereafter
157 referred to as EP-volume) that cover the study areas plus a margin and a depth range of 0-800 km. The margin
158 width is determined by the epicentral distance of the earthquake with varies from 8° to 3° in the distance range
159 of 30°-90°. We employed the *IASP91* model to compute the traveltimes of the grids at the boundaries of the
160 volume and applied the FMM to the *FWEA18* model to compute the 3-D P-wave traveltimes within the volume,
161 $T_P(l,m,n)$, which were stored as the traveltime table for interpolation. (2) For each station, we applied the FMM
162 to *FWEA18* to calculate a 3-D S-wave traveltime table ($T_S(i,j,k)$) for another 3-D volume (RS-volume), which is
163 centered at the station with a lateral dimension of 6°×6° and extends from surface to 800 km deep. When we
164 computed the two traveltime tables, we employed a cell size of 0.05° and 5 km in the horizontal and vertical
165 directions, respectively. (3) For every RF, we computed the absolute traveltime of *Pds* (t_{Pds}) and the direct P
166 (t_{P_0}), as well as the *Pds* relative traveltime with respect to P ($\Delta t_{Pds} = t_{Pds} - t_{P_0}$) through a linear interpolation
167 of the two 3-D traveltime tables. We employed the 1-D *Pds* conversion point location of the *IASP91* model as
168 an approximation in computing Δt_{Pds} . We further modified these steps to facilitate parallel computation; details
169 of the modification can be found in Zhang et al. (2022).

170 2.4. CCP stacking

171 To perform CCP stacking, we first digitized the rectangular study area of 100°-124°E, 18°-30°N with a set
172 of 0.1°×0.1° grids, resulting in a total of 29,161 (241×121) grids. For each grid, we set up a circular bin centered
173 at the grid with a radius of 1 degree and gathered all the RFs within the bin. Hereafter we refer to the number of
174 RFs in a bin as the hit count of the bin. Figures 2c and 2d show the hit counts at depths of 410 and 660 km,
175 respectively. If a bin has a hit count ≥ 150 , we stacked all the RFs within the bin using a 0.2 s long time window
176 centered at *Pds* traveltime (Δt_{Pds}). We varied the conversion depth, d , from 300 km to 800 km with an increment
177 of 1 km. It should be noted here that the 3-D image volume (100°-124°E, 18°-30°N, 300-800 km) is different
178 from the EP-volumes and RS-volumes used in computing the P- and S-wave traveltime tables, respectively. We
179 used two sets of *Pds* traveltimes (Δt_{Pds}^{IASP91} and Δt_{Pds}^{FWEA18}), one computed from the 1-D *IASP91* model and
180 another from the 3-D *FWEA18* model, to migrate the RF data.

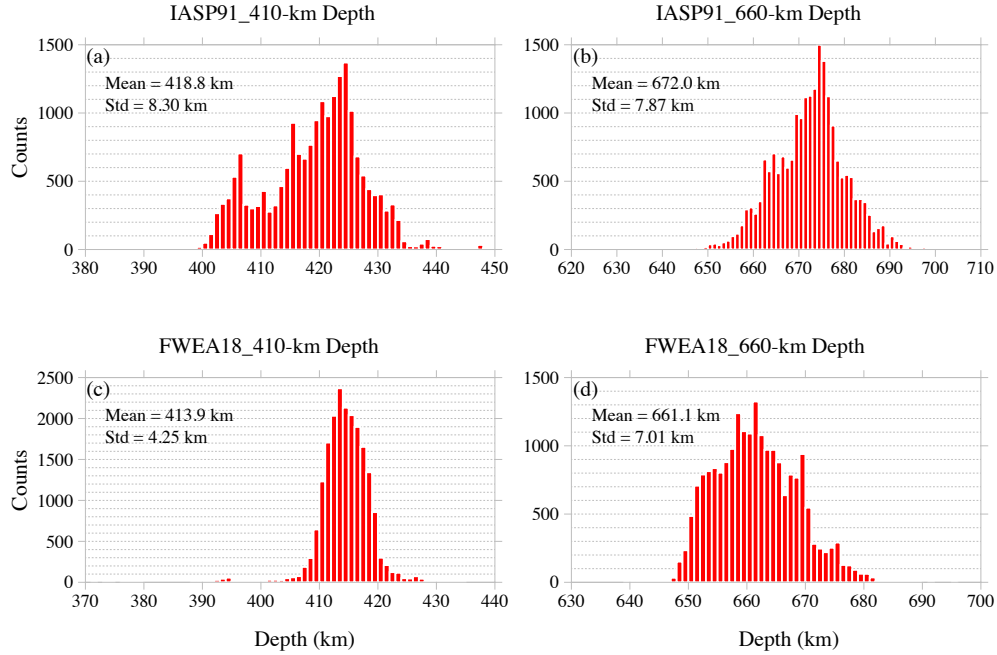
181 3. Results

182 3.1. Calibration of FMM with raytracing the *IASP91* model

183 To verify the accuracy of the FMM method in computing *Pds* traveltimes, we employed the 1-D *IASP91*
 184 model to conduct calibration tests using the raytracing method. For each RF, we calculated the 1-D traveltimes
 185 of P410s and P660s using the raytracing ($\Delta t_{P410s}^{IASP91_RT}$, $\Delta t_{P660s}^{IASP91_RT}$) and FMM ($\Delta t_{P410s}^{IASP91_FMM}$, $\Delta t_{P660s}^{IASP91_FMM}$)
 186 methods, and further computed their absolute differences ($\delta t_{P410s}^{IASP91} = |\Delta t_{P410s}^{IASP91_RT} -$
 187 $\Delta t_{P410s}^{IASP91_FMM}|$, $\delta t_{P660s}^{IASP91} = |\Delta t_{P660s}^{IASP91_RT} - \Delta t_{P660s}^{IASP91_FMM}|$). The P410s traveltime differences ($\delta t_{P410s}^{IASP91}$) of all
 188 the 49,592 RFs lie within 0.1 s, with an average and standard deviation of 0.027 and 0.019 s (Figure S2a).
 189 Similarly, all the P660s traveltime differences ($\delta t_{P660s}^{IASP91}$) fall within a 0.2 s range, with an average and standard
 190 deviation of 0.067 and 0.035 s (Figure S2b). We also confirmed the similarity of all the *Pds* times in the depth
 191 range of 300 km to 800 km and concluded that the FMM method provides an accurate way in computing *Pds*
 192 traveltimes.

193 3.2. CCP stacking with the 1-D *IASP91* model

194 We organized the 3-D image volumes into depth profiles at each of the $0.1^\circ \times 0.1^\circ$ grids. Due to the large
 195 number of RFs used in the CCP stacking, almost all the profiles showed clear P410s and P660s. We manually
 196 picked the depths of the two conversion signals from depth profiles. More specifically we tried to pick the P410s
 197 and P660s within the depth ranges of 380-440 km and 640-690 km, respectively. Figures 3a and 3b show the
 198 histograms of the depths to the 410-km and 660-km. The 410-km varies from ~400 to 440 km, with an average
 199 depth of 418.8 km and a standard deviation of 8.30 km, while the 660-km is located in the depth range of 650 to
 200 692 km, with an average of 672.0 km and a standard deviation of 7.87 km. Figures 4a and 4b display the lateral
 201 variations of depths to the 410-km and 660-km derived from *Pds* traveltimes calculated with the 1-D *IASP91*
 202 model, and Figure 4c shows the lateral variations of MTZ thickness, which is the depth difference of the two
 203 discontinuities. The 410-km exhibits an apparent depth of ≥ 420 km in a large area covering the entire Cathaysia
 204 Block and the SE Tibet but is shallower than ~400 km beneath the Yangtze Craton (Figure 4a). The southeastward
 205 dipping trend in apparent depth of the 410-km is also seen in the apparent depth to the 660-km discontinuity
 206 (Figure 4b). The apparent depth of the 660-km beneath the southeastern part of the study area is greater than 670
 207 km but is less than 660 km beneath the Yangtze Craton. The similar trend in the depth of the two discontinuities
 208 may also suggests that the upper mantle velocity beneath the Cathaysia Block is lower than that beneath the
 209 Yangtze Craton. The apparent MTZ thickness is relatively thin beneath the Cathaysia Block and southeastern
 210 edge of the Yangtze Craton. The MTZ beneath the Hainan volcanoes and the Qiongzhou Strait is ~240 km thick,
 211 ~10 km thinner than the global average. The MTZ beneath the SE Tibet and western Yangtze Craton is, however,
 212 ~10 km thicker than the global average.

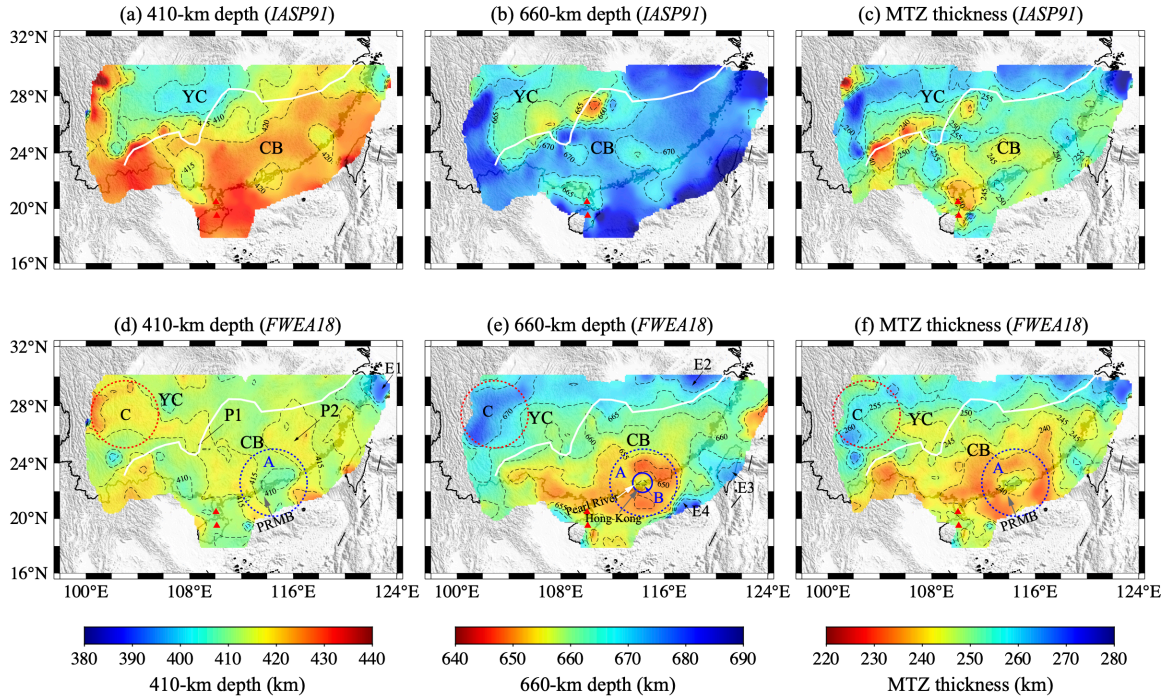


213

214 **Figure 3.** Histograms of the depth to the 410-km (a) and the 660-km (b) estimated from each circular bin with a hit count ≥ 150
 215 using the 1-D *IASP91* model as the reference model based on FMM. Std: standard deviation. (c) and (d) are the same as (a) and (b)
 216 except for the reference model, which is the 3-D *FWEA18* model.

217 **3.3. CCP stacking with the 3-D *FWEA18* model**

218 In the time-to-depth conversion of *Pds*, there is a tradeoff between the conversion depth and the upper
 219 mantle velocity. The measured depths of the two discontinuities thus can be biased by unmodeled 3-D velocity
 220 structures in the upper mantle and MTZ that are absent in the 1-D *IASP91* model. This is clearly shown in the
 221 *Pds* traveltimes calculated with the *IASP91* (Δt_{Pds}^{IASP91}) and the *FWEA18* (Δt_{Pds}^{FWEA18}) models. Figures S2c and
 222 S2d show the absolute traveltime differences of P410s ($\delta t_{P410s} = |\Delta t_{P410s}^{IASP91} - \Delta t_{P410s}^{FWEA18}|$) and P660s ($\delta t_{P660s} =$
 223 $|\Delta t_{P660s}^{IASP91} - \Delta t_{P660s}^{FWEA18}|$), respectively. δt_{P410s} has a maximum of ~ 3 s with an average and standard deviation of
 224 0.850 and 0.487 s, respectively. Meanwhile, δt_{P660s} shows a maximum of ~ 4 s with an average and standard
 225 deviation of 1.278 and 0.741 s.



226

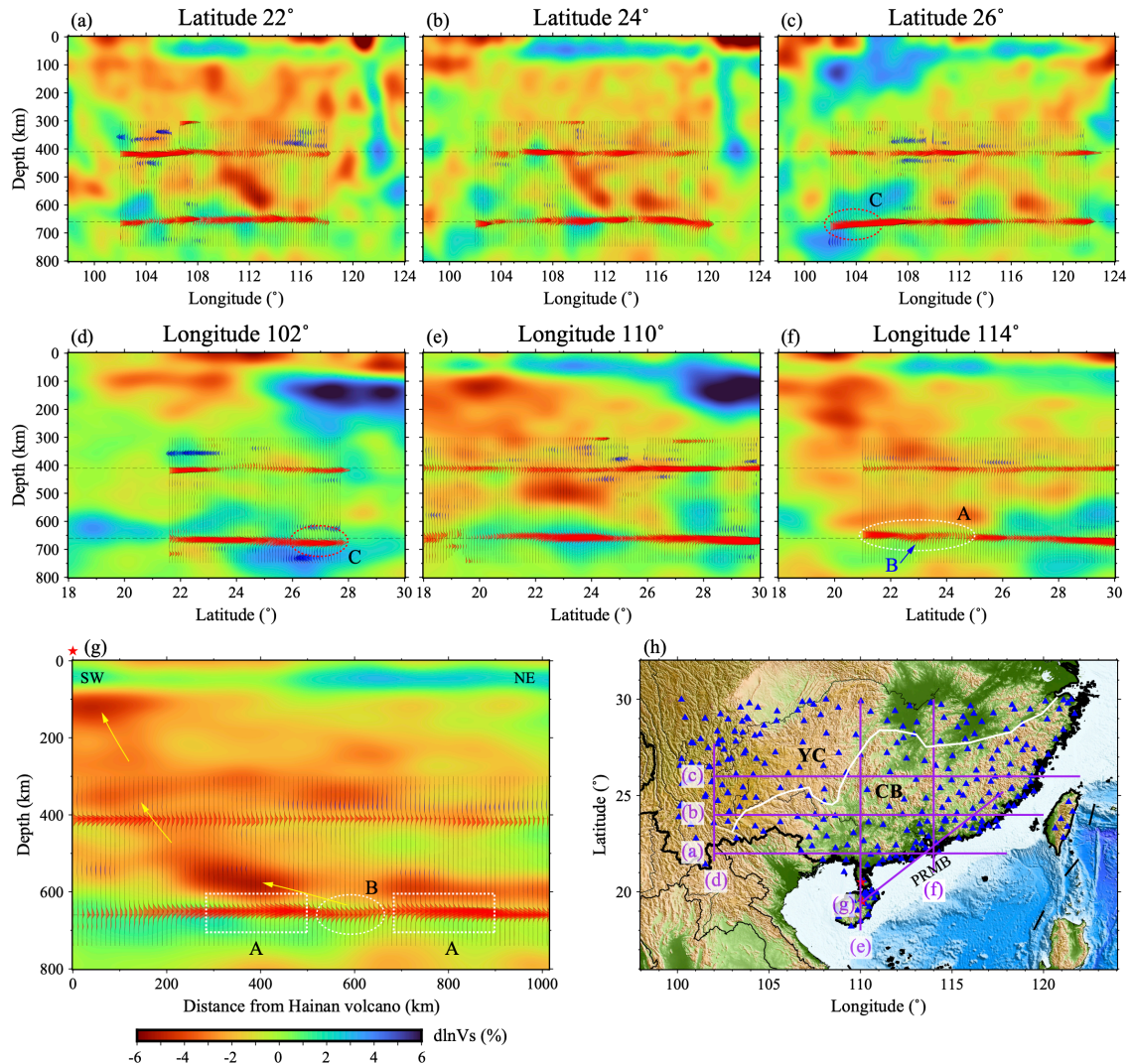
227 **Figure 4.** Color contour maps showing lateral variations in the depth to the 410-km (a) and to the 660-km (b), as well as in the
 228 thickness of the MTZ (c). The color scales are shown at the bottoms of each panel. Depths and thickness are estimated with a time-
 229 to-depth conversion computed from the 1-D *IASP91* model. (d)-(f) are the same as (a)-(c) except for the reference model which is
 230 the 3-D *FWEA18* model, used in computing the time-to-depth conversion. P1, P2, A, B, and C denote anomalies mentioned in the
 231 main text. E1-E4 are the anomalies located at the edge of the study area and are not discussed in the main text. YC: Yangtze Craton;
 232 CB: Cathaysia Block; PRMB: Pearl River Mouth Basin.

233 Figures 3c and 3d show the histograms of the depths to the 410-km and 660-km measured with the *FWEA18*
 234 model. The 410-km depth varies from 393 to 427 km, with an average of 413.9 km and a standard deviation of
 235 4.25 km (Figures 3c), and the 660-km depth ranges from 646 to 685 km, with an average of 661.1 km and a
 236 standard deviation of 7.0 km (Figure 3d). Both depths are significantly different from those measured with the
 237 *IASP91* model (Figures 3a and 3b). In particular, we noticed that standard deviation of the depth to the 410-km
 238 is almost half as 1-D estimates.

239 Figures 4d and 4e show mapviews of the depth to the 410-km and 660-km obtained by the 3-D model,
 240 which are also significantly different from those estimated with the 1-D model. The maximum depth change of
 241 the 660-km is approximately 40 km, corresponding to the ~4 s maximum difference in the P660s traveltime
 242 calculated with the two models. The 3-D results revealed that the 410-km is predominantly characterized by
 243 depressions ranging from 5 to 15 km with a few small uplifted patches (Figure 4d). Notably, there are two
 244 nearly parallel depression zones along the NW-SE direction on the topographic map of the 410-km (P1, P2 in
 245 Figure 4d). In contrast, the 660-km in the northwestern part of the study region is significantly deeper compared
 246 to the southeastern part (area C in Figure 4e). Additionally, the northern area of the Yangtze Craton exhibited a

247 large-scale depression of the 660-km, with a magnitude ranging from 10 to 25 km. There is a broad region
248 covering the southwestern half of the Cathaysia Block and its coastal area that shows an uplifted 660-km with
249 an amplitude of 5 to 15 km (area A in Figure 4e). In the middle of the uplifted area A, the 660-km has a low
250 topography with an almost normal depth, which is noted by B in Figure 4e. The depression seems to peak at the
251 central part of the Pearl River Mouth Basin (PRMB) near Hong Kong and is denoted as B in Figure 4e. We also
252 noticed that several high-amplitude anomalies are located at the edges of the study region, for example, E1
253 (Figure 4d) and E2 (Figure 4e) in the northeast corner and E3 and E4 (Figure 4e) at the southeast edge. Since
254 they are relatively less well sampled by our RF dataset, we decide not to interpret them in this study as the results
255 require further verification.

256 To further show the lateral depth variations of the two discontinuities, we further showed 7 depths profiles
257 of the CCP stacking in Figure 5, including 3 E-W profiles along latitude 22°N, 24°N and 26°N, 3 N-S profiles
258 along longitude of 102°E, 110°E and 114°E, and one NE-SW profile across the Hainan volcanic zone and PRMB.
259 The locations of the 7 profiles are indicated in Figure 5h. In each profile, we also showed the S-wave velocity
260 perturbations of the *FWEA18* model. All the profiles showed clearly P410s and P660s, allowing accurately
261 picking the depths of the two discontinuities. These profiles also clearly showed the major features about the
262 two discontinuities revealed by Figure 4: (1) most of the profiles exhibit a slightly depressed 410-km; (2) the
263 660-km at the western part of the 26°N profile and the northern part of the 102°E profile (C in Figures 5c and
264 5d) located beneath the western Yangtze Craton are depressed by a maximum of ~25 km, and the area with a
265 depressed 660-km shows a high S-wave velocity; (3) the annular shaped uplifting of 660-km beneath the
266 southern part of the Cathaysia Block is clearly visible along the 114°E profile (Figure 5f) and the SW-NE profile
267 (Figure 5g) and the uplift is surrounded by low-velocity anomalies.



268

269 **Figure 5.** (a), (b) and (c) show three E-W depth profiles of the CCP stackings (solid black lines) along latitude 22°N, 24°N, and
 270 26°N. S-wave velocity perturbations of the *FWEA18* model are also shown on the profiles for comparison. Red and blue colors
 271 denote the positive and negative anomalies, respectively. The two horizontal dashed lines denote the reference depths of 410 km
 272 and 660 km. (d), (e), and (f) are the N-S depth profiles along longitude 102°E, 110°E and 114°E. (g) is a depth profile along the
 273 NE-SW direction with an origin aligning with the volcano on the Hainan Island (red star on the top left of the profile). Yellow
 274 arrows show the plausible flow direction of the southwest branch. The areas marked with A, B, and C correspond to those in Figure
 275 4. (h) Topographic map showing the geographic locations of the 7 profiles (solid purple lines) and the seismic stations used in the
 276 study. PRMB: Pearl River Mouth Basin.

277 Figure 4f shows the lateral distribution of the MTZ thickness estimated from the *FWEA18* model. Compared
 278 to the depths to the two discontinuities, the MTZ maps estimated from *IASP91* and *FWEA18* models displayed
 279 more similarities albeit with some disparities in degree and extent. The MTZ thickness ranges from 221 to 270
 280 km, with an average value of approximately 247.3 km (Figure 4f). As indicated in Figure 3c, the 410-km exhibits

281 a smaller lateral variation than the 660-km. Therefore, the MTZ thickness map is primarily determined by
 282 fluctuations in the depth of the 660-km. The MTZ is much thicker in the western and northern parts of the study
 283 area and becomes thinner in the central and southeastern parts of the study region. The variations in the MTZ
 284 thickness beneath the Yangtze Craton and Cathaysia Block align coherently with velocity anomalies in the MTZ
 285 of the *FWEA18* model (Figure S3). A significant proportion of the high-velocity anomalies are situated in the
 286 northwestern part of the study area, which corresponds to the thickening of the MTZ. Conversely, in the
 287 southeastern region, large-scale low-velocity anomalies are observed, correlating with a thinning of MTZ.

288 4. Discussion

289 It has been known that a ground truth reference velocity model is critical in correctly positioning events in
 290 migration of seismic data. In the case of imaging MTZ with RFs, P- and S-wave velocity models with similar
 291 accuracy and resolution are required to obtain the ground truth depths of the 410-km and 660-km. The early RF
 292 studies of the South China Block used 1-D reference models (e.g., Ai et al., 2007). Huang et al. (2015) employed
 293 a 3-D S-wave velocity model and a scaled P-wave velocity model by assuming a fixed $\delta \ln V_s / \delta \ln V_p$. We thus
 294 believe there is a need of employing a high-resolution P- and S-wave velocity model to better image the 410-km
 295 and 660-km beneath the South China Block, We further argue that *FWEA18* fits the need as a reference model
 296 for RF imaging, since the P- and S-wave velocity models possess the similar spatial resolution and ground truth
 297 quality as V_p and V_s were inverted simultaneously from full waveform data including both body and surface
 298 waves.

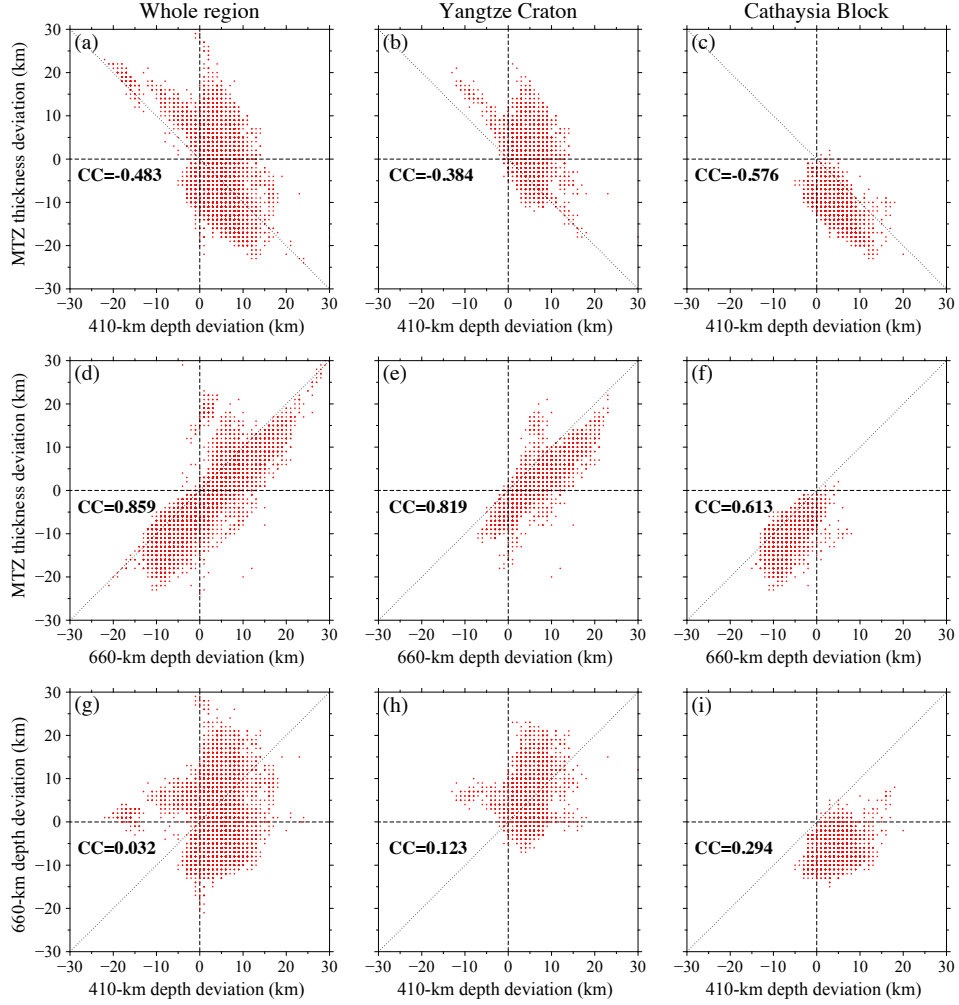
299 A ground truth velocity model can lead to constructive stacking of the P410s and P660s waves, resulting in
 300 high amplitudes of the two phases. Thus, the amplitude ratio of the two phases between RF images migrated
 301 with different reference models is an index to evaluate the quality of a reference model. To do so, we first
 302 measured the amplitudes of P410s and P660s from CCP stacking profiles based on the *IASP91* ($A_{P410s}^{IASP91}, A_{P660s}^{IASP91}$)
 303 and *FWEA18* ($A_{P410s}^{FWEA18}, A_{P660s}^{FWEA18}$) models, and then computed their ratios ($AR_{P410s} = A_{P410s}^{FWEA18} / A_{P410s}^{IASP91}$,
 304 $AR_{P660s} = A_{P660s}^{FWEA18} / A_{P660s}^{IASP91}$). Figures S4a and S4b show the histograms of the P410s and P660s amplitude
 305 ratios; Over 60% and 90% of the profiles showed an amplitude ratio >1 and >0.9 , respectively. A map view of
 306 the two amplitude ratios (Figures S4c and S4d) also suggested that most of the study area showed a similar or
 307 an increased amplitude of P410s and P660s with the *FWEA18* model. For these reasons, our discussion and
 308 interpretation of MTZ structure in the following sections will be based on the CCP images derived from the
 309 *FWEA18* model.

310 4.1. Reconcile depth variations of the two discontinuities and velocity anomalies to MTZ thermal 311 structures

312 To better constrain the origin of the topography of the 410-km and 660-km, we conducted a quantitative
313 comparison with the P- and S-wave velocity anomalies in the MTZ shown in the *FWEA18* model. More
314 specifically, we would like to investigate whether temperature anomalies are the primary cause of the observed
315 the depth and velocity anomalies. Although SS precursor studies (Flanagan & Shearer, 1998; Gu & Dziewonski,
316 2002) suggested the global averaged depths of the two discontinuities are 418 km and 660 km, respectively, we
317 still used 410 km and 660 km as the reference depths to computed depth anomalies of the two discontinuities.
318 The average depths of the 410-km and 660-km are 413.9 km and 661.1 km, resulting in an average MTZ
319 thickness of 247.3 km beneath the study region.

320 As shown in the previous section, the MTZ exhibits different structures beneath the Yangtze Craton and the
321 Cathaysia Block. Thus, we chose two rectangular areas that have high hit counts of RF data, (100°-110°E, 24°-
322 30°N) from the Yangtze Craton and (110°-118°E, 20°-26°N) from the Cathaysia Block, for more detailed
323 comparison. The two areas are outlined in Figure 2. The average depths of the 410-km beneath the two areas
324 are identical: 414.8 km for the Yangtze Craton and 414.8 km for the Cathaysia Block. These values closely
325 resemble the overall average depth of the 410-km in the whole South China Block, indicating a widespread
326 depression throughout the study area. The average 660-km depth beneath the Yangtze Craton is 666.4 km, and
327 is 654.1 km beneath the Cathaysia Block, resulting in a difference of approximately 12 km.

328 If the observed depth anomalies are caused by temperature-sensitive phase transitions of the upper mantle
329 minerals, and if there are thermal anomalies extending the entire MTZ, then we would expect to observe
330 correlations/anticorrelations among the depths of the two discontinuities as well as the MTZ thickness. If phase
331 transitions of olivine are the major causes of the two seismic discontinuities, then there is an anticorrelation
332 between the depths of the 410-km and 660-km. In Figure 6, we plot the deviations of MTZ thickness versus the
333 410-km depth, MTZ thickness versus the 660-km depth, and 410-km depth versus the 660-km depth beneath the
334 whole region, the Yangtze Craton, and the Cathaysia Block. The 410-km depth beneath the Cathaysia Block
335 (Figure 6c) displays a stronger negative correlation with the MTZ thickness than that beneath the Yangtze Craton
336 (Figure 6b). Meanwhile, there is a strong positive correlation between the MTZ thickness and the 660-km depth
337 across the entire study area (Figure 6d), including the Yangtze Craton (Figure 6e) and Cathaysia Block (Figure
338 6f). The correlation between the depths of the 410-km and the 660-km is relatively low (Figures 6g-6i), with the
339 highest of 0.294 from the Cathaysia Block (Figure 6i). Based on these observations, we speculated that the
340 thicker MTZ beneath the Yangtze Craton is primarily caused by a depressed 660-km, which is likely originated
341 from low temperature. This thermal anomaly also does not seem to extend throughout the entire MTZ. In
342 comparison, the high temperature anomalies within the MTZ below the Cathaysia Block are widespread across
343 the transition zone, affecting both the 410-km and 660-km topographies.



344

345 **Figure 6.** The MTZ thickness perturbations are shown as a function of the depth variations of the 410-km measured in the entire
 346 study region (a), the Yangtze Craton (b), and the Cathaysia Block (c). The dotted line with a negative slope represents a perfect
 347 anticorrelation, and CC indicates the calculated cross-correlation coefficient between the two datasets. (d), (e), and (f) are the same
 348 as (a), (b) and (c) except for the depth variations of the 660-km. The dotted line with a positive slope represents a perfect correlation,
 349 and CC indicates the calculated cross-correlation coefficient between the two datasets. (g-i) The depth variations of the 660-km are
 350 shown as a function of the depth variations of the 410-km measured in the three regions. The dotted line with a positive slope
 351 represents a perfect correlation between, while CC indicates the calculated cross-correlation coefficient between the two datasets.

352 To estimate temperature anomalies associated with the observed depths of the two discontinuities, we first
 353 computed the temperature sensitivity of the depth to the 410-km and 660-km (Helffrich, 2000):

$$354 \quad \delta T / \delta z_{410} = \left(\frac{dP}{dz} \right)_{410} / \left(\frac{dP}{dT} \right)_{410} = \rho_{410} g / \left(\frac{dP}{dT} \right)_{410} \quad (1a)$$

$$355 \quad \delta T / \delta z_{660} = \left(\frac{dP}{dz} \right)_{660} / \left(\frac{dP}{dT} \right)_{660} = \rho_{660} g / \left(\frac{dP}{dT} \right)_{660} \quad (1b)$$

356 Here $(dP/dT)_{410}$ and $(dP/dT)_{660}$ are the Clapeyron slopes of the olivine-to-wadsleyite and ringwoodite-to-
357 perovskite phase transitions, respectively. By using $(dP/dT)_{410}=2.7\pm0.3$ MPa/K and $(dP/dT)_{660}=-2.6\pm0.5$ MPa/K
358 (e.g., Bina and Helffrich, 1994; Akaogi et al., 2007), $\rho_{410}=3.634$ g/cm³, $\rho_{660}=4.186$ g/cm³, and $g=10$ m/s², we
359 obtained the depth-temperature sensitivity of the 410-km and 660-km to be $\delta T/\delta z_{410}=13.6\pm1.5$ K/km and
360 $\delta T/\delta z_{660}=-16.6\pm3.1$ K/km, respectively.

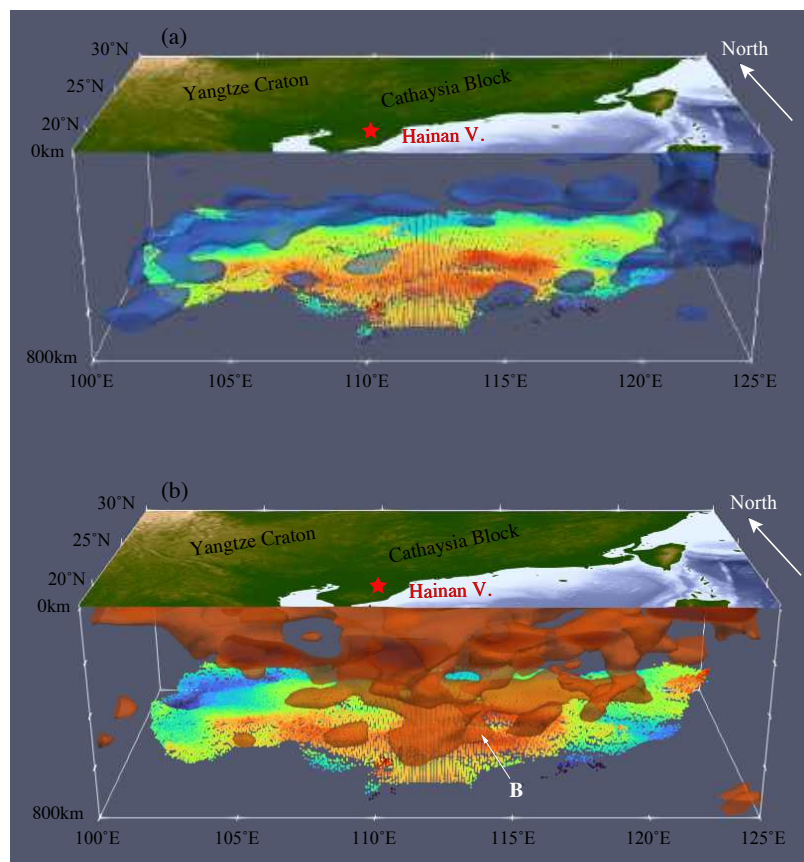
361 Using the above scaling relationship, we converted the maximum 15 km depression of the 410-km beneath
362 western Yangtze Craton (area C in Figure 4d) to an elevated mantle temperature of 182-227 K. Similarly, the
363 deepened 660-km by 20 km observed beneath the same region ((area C in Figure 4e) corresponds to a cold
364 surrounding mantle with a relative temperature of -270 to -394 K. On the other hand, the temperature in the P1
365 and P2 areas (Figures 4d) of the Cathaysia Block is uplifted by ~5 km, corresponding to a mantle warmer by 61-
366 76 K in temperature. The broad uplift of 660-km beneath the southern Cathaysia Block with a peak amplitude
367 of 15 km (area A in Figure 4e) can be resulted from a hotter-than-normal mantle with temperature anomaly of
368 203-296 K. We further converted these temperature anomalies to P- and S-wave velocity perturbations based on
369 their temperature sensitivities ($(\partial \ln V_s / \partial T)_{410}$, $(\partial \ln V_s / \partial T)_{410}$; $(\partial \ln V_s / \partial T)_{660}$, $(\partial \ln V_s / \partial T)_{660}$) estimated
370 by Cammarano et al. (2003). The calculated velocity perturbations are listed in Table S1. These values are
371 roughly comparable to those of the *FWEA18* model (Figure S3). However, the temperature-converted S-wave
372 perturbations at 410 km beneath the Yangtze Craton and at 660 km beneath the Cathaysia Block are much larger
373 than those in the *FWEA18* model. We further computed the correlation between depth variations of the two
374 discontinuities and S-wave velocity perturbations ($d \ln V_s$) of *FWEA18* at each grid (Figure S5). In general, the
375 correlation between the two are not so obviously (Figure S5), which may suggest temperature anomalies might
376 not be the sole cause of the observed velocity and depth perturbations. The low correlation could also be caused
377 by errors in the depth and velocity estimates.

378 4.2. Slab segments within the MTZ

379 The most prominent area with a depressed 660-km is in the Yangtze Craton region (region C in Figure 4e),
380 except for the northeastern corner and southeastern edge of the study area (E2, E3, and E4 in Figure 4e), which
381 need further verification with more data. At the C area, the maximum depression of the 660-km is ~25 km
382 compared to the global average (660 km). The most plausible explanation for this depression is the presence of
383 low temperature structures, which are imaged as high velocity bodies around the 660-km by many tomographic
384 studies (e.g., Sun et al., 2016; Zhang et al., 2017; Tao et al., 2018). Various interpretations have been offered to
385 the possible origin of the high velocity anomalies, such as detached lithosphere (e.g., Zhang et al., 2017), the
386 eastward subducting Indo-Burma slab (e.g., Xu et al., 2018), and the stagnant slab of the Paleo- Pacific plate
387 (e.g., Sun et al., 2016). Our CCP stacking images showed that the 660-km in the C area has a maximum
388 depression of 25 km, suggesting that the mantle at the base of the MTZ in the C area is ~337-492 K colder than

389 its adjacent areas. This temperature difference could result in 2-3% perturbations in P-wave velocity and 5-7%
390 perturbations in S-wave velocity, which is consistent with the *FWEA18* model (Figure S3).

391 Our CCP stacking images, however, do not offer additional constraints on the origin of the high velocity
392 anomalies, as the depth of the 660-km is affected by not only temperature but also water content (e.g., Higo et
393 al., 2001; Litasov et al., 2005). The 3-D perspective view of high velocity anomalies of the *FWEA18* model
394 beneath the study area (Figure 7a) indicates that the high velocity anomalies across the 660-km in the C area is
395 an isolated structure, without obvious connection with the subducting high-velocity slabs of the Philippine Sea
396 plate from the east and the India plate from the west. Since the northern part of the depression is located beneath
397 the southern Sichuan Basin where the cratonic lithosphere is expected to be intact as a high velocity anomaly
398 down to ~200 km deep is visible from many tomographic models (e.g., Tao et al., 2018), geometrically it is
399 difficult to attribute the high velocity structures to the delaminated continental lithosphere. The depression is
400 elongated along the NE-SW direction, which may imply for a piece of slab being subducted from either the
401 southeast or the northwest. Therefore, we favor more on an origin related to the Paleo-Pacific subduction.



402
403 **Figure 7.** 3-D illustration of the (a) high ($dlnVs \geq 2.0\%$) and (b) low ($dlnVs \leq -2.0\%$) velocity bodies of the *FWEA18* in the
404 depth range of 0-800 km beneath the SCB region. The colored map shown at the bottom of each 3-D illustration represent the 660-
405 km topography, which is the same as the Figure 4c.

406 4.3. Upwelling of the Hainan plume

407 Compared to the Yangtze Craton, the Cathaysia Block region has experienced more active magmatic activity
408 (e.g., Zhou and Li, 2000). Several studies suggest that the magmatic activity in this region may be associated
409 with either lateral mantle flow resulting from plate collision (e.g., Liu et al., 2004) or mantle wedge circulation
410 related to plate subduction (e.g., Maruyama et al., 2009). Lebedev et al. (2000) employed tomography to identify
411 a low velocity zone surrounding the Hainan Island, which was subsequently designated as the Hainan plume.
412 The mantle plume hypothesis, which involves the transport of hot materials from the deep mantle, has been
413 effectively applied to explain intraplate magmatism in various locations with hotspots. Nevertheless, the precise
414 location where the Hainan plume enters the MTZ, along with its connection with the Hainan volcanoes in the
415 upper mantle, remain unknown.

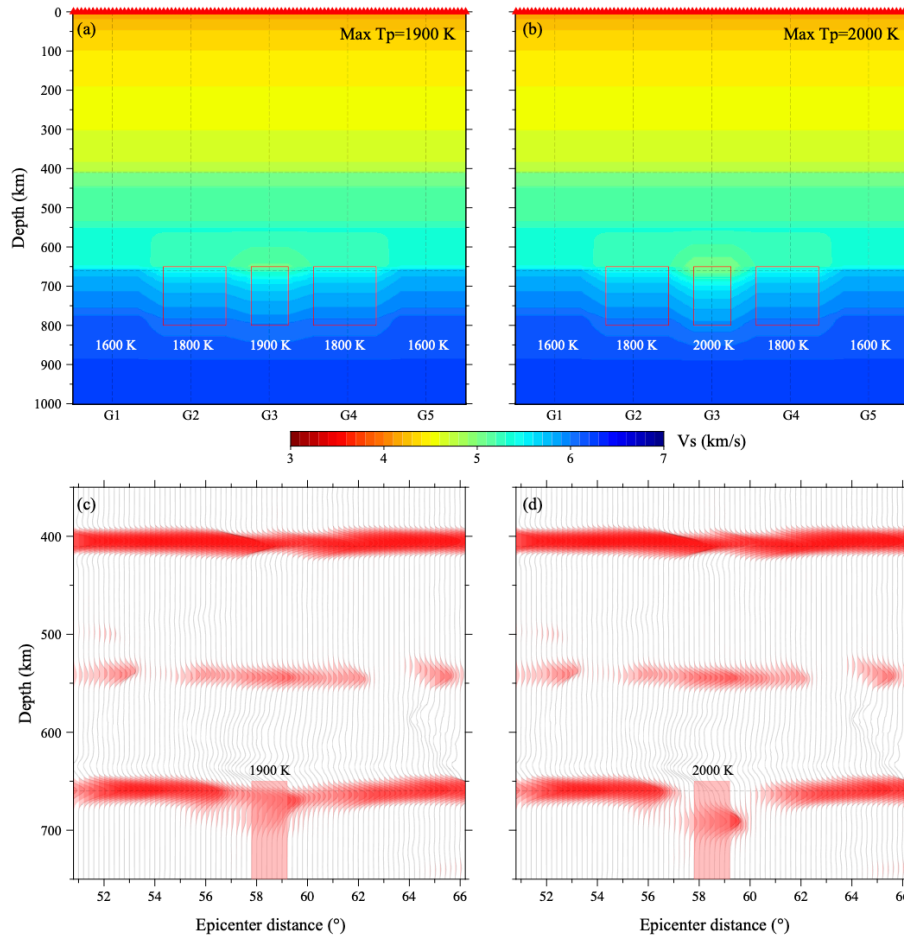
416 Both global and local seismic travelttime tomography have been utilized to investigate the deep structure
417 beneath this region. Some findings indicate that mantle upwelling may be rooted within the MTZ, while others
418 propose that it may originate from the core-mantle boundary (e.g., Huang & Zhao, 2006; He & Santosh, 2021).
419 Huang (2014) observed a low velocity anomaly beneath the Hainan volcanoes which tilts toward northeast and
420 extends to 700 km deep. The shape of the low velocity anomaly does not fall into a classic image of mantle
421 plume which ascends vertically from deep mantle. Xia et al. (2016) proposed a mushroom-like continuous low
422 velocity anomaly, which is characterized by a narrow columnar tail extending from the lower mantle beneath
423 northeastern part of the Hainan hotspot and a broad head spreading laterally within and around the MTZ.
424 Regarding where the Hainan plume enters to the MTZ from the lower mantle, studies utilizing RFs to image the
425 thinning position of the MTZ have produced multiple results. Some researchers proposed that the intersection of
426 the Hainan plume and the MTZ occurs beneath the Qiongzhou Strait (Huang et al., 2015), while others suggested
427 it is to the northeast of the Hainan Island, somewhere at the coastal area of the Guangdong Province (Wei &
428 Chen, 2016).

429 In this study, we found a significant uplift of the 660-km beneath the southern Cathaysia Block (Figure 4e),
430 which also displays notable thinning of the MTZ thickness (Figure 4f). The most prominent uplift area sits in
431 the coastal region to northeast of the Hainan volcanos (A in Figure 4e). One possible explanation of the uplift is
432 the presence of a mantle plume in the area. A close look of the broad uplift also revealed its annular shape with
433 a low area that is centered at 114.2° E and 22.6° N (near Hong Kong in Figure 1b) with a diameter of
434 approximately 150 km. The 660-km in the area displays a depression relative to the surrounding uplifted areas,
435 which is labelled as B in Figure 4e. The depth profile shown in Figure 5g extending from the Hainan Island
436 reveals a 660-km with an undulation of uplift-depression-uplift from SW to NE. Figure 7b shows 3-D distribution
437 of low velocity anomalies of the *FWEA18* model beneath the study area. We found the B area is at the center of
438 a large low velocity anomaly in the MTZ which seems to extend to the lower mantle, suggesting a scenario that
439 hot material arising from the lower mantle enter the transition zone at the B area and then spread horizontally

440 within the MTZ. The hot materials continue to rise and evolve into two branches corresponding to the two nearly
441 parallel depression zones of the 410-km (P1, P2 in Figure 4d). The major branch keeps moving upward to the
442 southwest and feeds the Hainan volcanos (yellow arrows in Figure 5g).

443 In general, the depth of the 660-km is mainly controlled by the phase transformation of olivine mineral, the
444 major constituent of upper mantle. However, in a substantially high temperature condition, phase transitions of
445 the non-olivine minerals, such as the majorite-garnet to perovskite transition, can play a major role in
446 determining seismic properties (Hirose, 2002). The majorite-garnet to perovskite transition has a positive
447 Clapeyron slope, meaning that a deeper, rather than a shallower 660-km is expected when mantle temperature is
448 significantly higher than the global mean. This indicates that in the presence of substantial high temperature
449 anomalies, the garnet phase transformation in mantle minerals may play a more important role, resulting in a
450 deeper, rather than shallower, seismologically observed 660-km. In fact, several previous studies have reported
451 a deepened 660-km within hot mantle beneath Kenya, Tanzania, and Hawaii that may be associated with mantle
452 plumes (Deuss, 2007; Huerta et al., 2009; Cao et al., 2011). Thus, we postulate that the B area has a mantle
453 temperature higher than its surroundings and the depression in the area is caused by the positive Clapeyron slope
454 of the majorite-garnet to perovskite transition.

455 To investigate this hypothesis, we generated 2-D synthetic models of mantle with a pyrolite composition
456 (Ringwood, 1962) and laterally varying geotherms. Since the garnet-perovskite phase change only occurs at
457 elevated temperatures above 200 to 300 K (Jenkins et al., 2016), we designed two 2-D models based on the
458 geometry of the NE-SW profile shown in Figure 5g: the first model with a lateral potential temperature (T_p)
459 variation of 1600-1800-1900-1800-1600 K (Figure 8a; maximum $T_p=1900$ K) and the second model with a
460 varying T_p of 1600-1800- 2000-1800-1600 K (Figure 8b; maximum $T_p=2000$ K). The lateral extensions of the
461 1800 K and 1900 K/2000 K segments are 200 km and 150 km, respectively, which are roughly similar to the
462 dimensions of A and B in the NE-SW profile (Figure 5g). We first employed `Perple_X` (Connolly, 2005) to
463 compute seismic velocities and density of the two 2-D models. The calculated S-wave velocity of the two models
464 is shown in Figures 8a and 8b, while the P-wave velocity and density of the two models are shown in Figures
465 S6a-S6d. We also showed depth profiles of V_p , V_s , and density at 5 grid points that represents the background
466 mantle, moderately hot and substantially hot mantle in Figure S7.

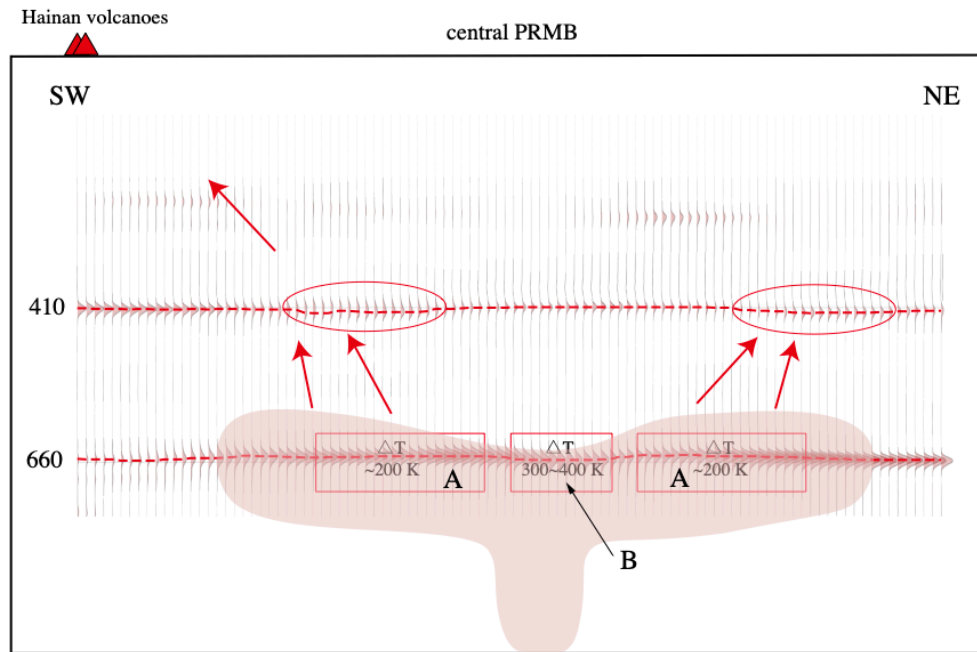


467

468 **Figure 8.** (a) A synthetic 2-D velocity profile showing S-wave velocity computed from a mineralogical model with a maximum T_p
 469 of 1900 K at the center. T_p decreases toward the edge with increments of 100 K and reaches 1600 K at the two edges of the profile.
 470 S-wave velocity is shown in color and the color scale is shown at the bottom of the profile. G1-G5 show the location of 5 grids
 471 with their 1-D velocity profile being shown in Figure S7. (b) is the same as (a) except for a maximum T_p of 2000 K at the center
 472 of the profile. Synthetic tests for the 660-km undulations under extremely high temperatures. (c) shows the CCP stacking of
 473 synthetic RFs computed with the 2-D velocity model shown in (a). Red color denotes the positive pulses and the light red rectangle
 474 represents maximum T_p of 1900 K region. (d) is the same as (c) except for a maximum T_p of 2000 K.

475 We then employed the 2-D finite-difference method (Li et al., 2014) to compute synthetic waveforms of the
 476 two models for all the event-receiver pairs using in the CCP stacking of the NE-SW profiles shown in Figure 5g.
 477 The resulting synthetic seismograms were processed in a similar manner to the real data to obtain RFs, which
 478 were subsequently employed in the CCP stacking. Results of the CCP stacking of the synthetic RFs of the two
 479 models are shown in Figures 8c and 8d. The 660-km of the two CCP images exhibits undulations comparable
 480 to the real data image. In the two edges away from the hot center, depth to the 660-km is close to normal (Figures
 481 8c and 8d). Both images show that the 660-km rises and then falls when it approaches to the center with
 482 increasing temperature. We noticed the depressions of the 660-km at the central area in the two synthetic images
 483 are much larger than that observed in the B area, suggesting either the Clapeyron slope used in the mineral

484 physical models are overestimated, or the ringwoodite to perovskite phase change of the olivine and water
485 content might have played a role of the observed 660-km in the B area.



486
487 **Figure 9.** Schematic illustration showing the deep origin of the Hainan plume and its pathway in the MTZ and upper mantle toward
488 the Hainan volcanoes in the surface. CCP stackings along the NE-SW profile shown in Figure 5g is also plotted for comparison.

489 Our results thus may suggest the Hainan volcanoes is likely fed by a displaced hot plume in the lower mantle.
490 The CCP images indicate the following scenario: a conduit of hot plume materials with a diameter of ~150 km
491 rises from the lower mantle and hits the 660-km at central Pearl River Mouth Basin near Hong Kong, which
492 shows as low velocity anomaly in the uppermost lower mantle and a depression of 660-km in the B area.
493 Temperature within the plume is ~300-400 K higher than that of a normal mantle at the same depths. Hot plume
494 materials accumulate at the base of MTZ and spread horizontally before progressing further toward the 410-km
495 as two rising channels of hot materials (Figure 9). While the minor branch moves upward to the northeast, the
496 major channel flows to the southwest, rising to the shallow depths and feeding the Hainan volcanoes at the
497 surface.

498 5. Conclusions

499 We conducted CCP migration of a large RF dataset with a 3-D high-resolution velocity model to image the
500 410-km and 660-km. By comparing velocity structures around the two discontinuities and numerical analyses
501 with synthetic models of mantle minerals and different geotherms, we reached the following conclusions: (1)
502 The 660-km beneath the western Yangtze Craton shows a 10-25 km depression and is surrounded by high-
503 velocity anomalies, suggesting that the depression is likely caused by a cold stagnant slab with higher-than-

504 normal seismic velocity. The NE-SW elongated shape of the depression may imply that the stagnant slab is
505 associated with the northwestward subducted Paleo-Pacific plate. The cold stagnant slab does not seem to reach
506 the upper part of the MTZ and affect the 410-km. (2) The 660-km beneath the southern part of the Cathaysia
507 Block is uplifted by 5-15 km in a broad area with a lateral extension of ~500-600 km. There is topographic low
508 at the central part of the plateau with a diameter of ~150 km. We attributed the topographic low to the positive
509 slope of the garnet-perovskite phase transition in hot mantle with an excess temperature of 300-400 K. By
510 integrating seismic observations and mineral physical modeling, we propose that Hainan plume has a displaced
511 origin in the lower mantle, which is located at the central PRMB near Hong Kong. Once the plume enters to
512 MTZ, it spreads horizontally and diverges into two channels, one minor branch toward the northeast, and a major
513 one toward the southeast. Both move upward and affect the 410. The southwest moving channel provides the
514 source that feeds the Hainan volcanoes.

515 **Acknowledgments**

516 We thank the Data Management Centre of the China National Seismic Network at the Institute of Geophysics,
517 China Earthquake Administration (SEISDMC, doi:10.11998/SeisDmc/SN) for providing the seismic data. The
518 earthquake catalog was downloaded from the U.S. Geological Survey (USGS). The figures were created with
519 the Generic Mapping Tools (GMT; Wessel et al., 2013) and Paraview (www.paraview.org). This work was
520 supported by the National Natural Science Foundation of China (No. 40274022) and (No. 41630209).

521 **Data Availability Statement**

522 Seismic data used in this study are available from the DMC repository of the China Earthquake
523 Administration (SEISDMC, doi:10.11998/SeisDmc/SN).

524

525 **References**

- 526 Ai, Y., Chen, Q., Zeng, F., Hong, X., Ye, W., 2007. The crust and upper mantle structure beneath southeastern China.
527 Earth and Planetary Science Letters, 260, 549-563. <https://doi.org/10.1016/j.epsl.2007.06.009>.
- 528 Akaogi, M., Takayama, H., Kojitani, H., Kawaji, H., Atake, T., 2007. Low-temperature heat capacities, entropies and
529 enthalpies of Mg₂SiO₄ polymorphs, and α - β - γ and post-spinel phase relations at high pressure. Physics and
530 Chemistry of Minerals 34, 169-183. <https://doi.org/10.1007/s00269-006-0137-3>.
- 531 Bina, C. R., Helffrich, G., 1994. Phase transition Clapeyron slopes and transition zone seismic discontinuity
532 topography. J. Geophys. Res. Solid Earth 99, 15853-15860. <https://doi.org/10.1029/94JB00462>.
- 533 Briaies, A., Patriat, P., Tapponnier, P., 1993. Updated interpretation of magnetic anomalies and seafloor spreading stages
534 in the south China Sea: Implications for the Tertiary tectonics of Southeast Asia. J. Geophys. Res. 98, 6299-6328.
535 <https://doi.org/10.1029/92JB02280>.
- 536 Cammarano, F., Goes, S., Vacher, P., Giardini, D., 2003. Inferring upper-mantle temperatures from seismic velocities.
537 Physics of the Earth and Planetary Interiors 138, 197-222. [https://doi.org/10.1016/S0031-9201\(03\)00156-0](https://doi.org/10.1016/S0031-9201(03)00156-0).
- 538 Cao, Q., Van der Hilst, R.D., De Hoop, M.V., Shim, S.H., 2011. Seismic imaging of transition zone discontinuities
539 suggests hot mantle west of Hawaii. Science 332, 1068-1071. <https://doi.org/10.1126/science.1202731>.
- 540 Clayton, R.W., Wiggins, R.A., 1976. Source shape estimation and deconvolution of teleseismic bodywaves.
541 Geophysical Journal International 47, 151-177. <https://doi.org/10.1111/j.1365-246X.1976.tb01267.x>.
- 542 Connolly, J. A. D., 2005. Computation of phase equilibria by linear programming: A tool for geodynamic modeling
543 and its application to subduction zone decarbonation. Earth and Planetary Science Letters 236, 524-541.
544 <https://doi.org/10.1016/j.epsl.2005.04.033>.
- 545 de Kool, M., Rawlinson, N., Sambridge, M., 2006. A practical grid-based method for tracking multiple refraction and
546 reflection phases in three-dimensional heterogeneous media. Geophysical Journal International 167, 253-270.
547 <https://doi.org/10.1111/j.1365-246X.2006.03078.x>.
- 548 Deuss, A., 2007. Seismic observations of transition-zone discontinuities beneath hotspot locations. in: Special Paper
549 430: Plates, Plumes and Planetary Processes. Geological Society of America Special Papers 430: 121-136.
550 [https://doi.org/10.1130/2007.2430\(07\)](https://doi.org/10.1130/2007.2430(07)).
- 551 Flanagan, M. P., Shearer, P.M., 1998. Global mapping of topography on transition zone velocity discontinuities by
552 stacking SS precursors. J. Geophys. Res. Solid Earth 103, 2673-2692. <https://doi.org/10.1029/97JB03212>.

553 Gu, Y.J., Dziewonski, A.M., 2002. Global variability of transition zone thickness. *J. Geophys. Res. Solid Earth* 107,
554 ESE-2. <https://doi.org/10.1029/2001JB000489>.

555 Guan, Z., Niu, F., 2018. Using Fast Marching Eikonal Solver to Compute 3-D Pds Traveltime for Deep Receiver-
556 Function Imaging. *J. Geophys. Res. Solid Earth* 123, 9049-9062. <https://doi.org/10.1029/2018JB015892>.

557 Han, R., Li, Q., Huang, R., Zhang, H., 2020. Detailed structure of mantle transition zone beneath southeastern China
558 and its implications for thinning of the continental lithosphere. *Tectonophysics* 789, 228480.
559 <https://doi.org/10.1016/j.tecto.2020.228480>.

560 He, C., Santosh, M., 2021. Mantle Upwelling Beneath the Cathaysia Block, South China. *Tectonics* 40.
561 <https://doi.org/10.1029/2020TC006447>.

562 Helffrich, G., 2000. Topography of the transition zone seismic discontinuities. *Rev. Geophys.* 38, 141-158.
563 <https://doi.org/10.1029/1999RG000060>.

564 Higo, Y., Inoue, T., Irifune, T., Yurimoto, H., 2001. Effect of water on the spinel-postspinel transformation in Mg₂SiO₄.
565 *Geophys. Res. Lett.* 28, 3505-3508. <https://doi.org/10.1029/2001GL013194>.

566 Hirose, K., 2002. Phase transitions in pyrolitic mantle around 670-km depth: Implications for upwelling of plumes
567 from the lower mantle. *J. Geophys. Res.* 107. <https://doi.org/10.1029/2001JB000597>.

568 Huang, H., Tosi, N., Chang, S., Xia, S., Qiu, X., 2015. Receiver function imaging of the mantle transition zone beneath
569 the South China Block. *Geochem. Geophys. Geosyst.* 16, 3666-3678. <https://doi.org/10.1002/2015GC005978>.

570 Huang, J., 2014. P- and S-wave tomography of the Hainan and surrounding regions: Insight into the Hainan plume.
571 *Tectonophysics* 633, 176-192. <https://doi.org/10.1016/j.tecto.2014.07.007>.

572 Huang, J., Zhao, D., 2006. High-resolution mantle tomography of China and surrounding regions. *J. Geophys. Res.*
573 111, B09305. <https://doi.org/10.1029/2005JB004066>.

574 Huang, R., Xu, Y., Luo, Y., Jiang, X., 2014. Mantle Transition Zone Structure Beneath Southeastern China and its
575 Implications for Stagnant Slab and Water Transportation in the Mantle. *Pure Appl. Geophys.* 171, 2129-2136.
576 <https://doi.org/10.1007/s00024-014-0837-4>.

577 Huerta, A.D., Nyblade, A.A., Reusch, A.M., 2009. Mantle transition zone structure beneath Kenya and Tanzania: more
578 evidence for a deep-seated thermal upwelling in the mantle. *Geophysical Journal International* 177, 1249-1255.
579 <https://doi.org/10.1111/j.1365-246X.2009.04092.x>.

580 Ita, J., Stixrude, L., 1992. Petrology, elasticity, and composition of the mantle transition zone. *J. Geophys. Res.* 97,
581 6849. <https://doi.org/10.1029/92JB00068>.

582 Jenkins, J., Cottaar, S., White, R.S., Deuss, A., 2016. Depressed mantle discontinuities beneath Iceland: Evidence of
583 a garnet controlled 660 km discontinuity? *Earth and Planetary Science Letters* 433, 159-168.
584 <https://doi.org/10.1016/j.epsl.2015.10.053>.

585 Katsura, T., Ito, E., 1989. The system Mg_2SiO_4 - Fe_2SiO_4 at high pressures and temperatures: Precise determination of
586 stabilities of olivine, modified spinel, and spinel. *J. Geophys. Res.* 94, 15663-15670.
587 <https://doi.org/10.1029/JB094iB11p15663>.

588 Kennett, B. L., Engdahl, E.R., 1991. Travel times for global earthquake location and phase identification. *Geophysical*
589 *Journal International* 105, 429-465. <https://doi.org/10.1111/j.1365-246X.1991.tb06724.x>.

590 Lebedev, S.S., Chevrot, S., Nolet, G., Van der Hilst, R., 2000. New seismic evidence for a deep mantle origin of the
591 S. China basalts (the Hainan plume?) and other observations in SE Asia. *Eos Trans. AGU* 81, 48.

592 Li, C., van der Hilst, R.D., 2010. Structure of the upper mantle and transition zone beneath Southeast Asia from
593 travelttime tomography. *J. Geophys. Res.* 115, B07308. <https://doi.org/10.1029/2009JB006882>.

594 Li, D., Helmberger, D., Clayton, R.W., Sun, D., 2014. Global synthetic seismograms using a 2-D finite-difference
595 method. *Geophysical Journal International* 197, 1166-1183. <https://doi.org/10.1093/gji/ggu050>.

596 Litasov, K. D., Ohtani, E., Sano, A., Suzuki, A., Funakoshi, K., 2005. Wet subduction versus cold subduction. *Geophys.*
597 *Res. Lett.* 32, L13312. <https://doi.org/10.1029/2005GL022921>.

598 Liu, M., Cui, X., Liu, F., 2004. Cenozoic rifting and volcanism in eastern China: a mantle dynamic link to the Indo-
599 Asian collision? *Tectonophysics* 393, 29-42. <https://doi.org/10.1016/j.tecto.2004.07.029>.

600 Liu, Z., Niu, F., Chen, Y. J., Grand, S., Kawakatsu, H., Ning, J., Tanaka, S., Obayashi, M., Ni, J., 2015. Receiver
601 function images of the mantle transition zone beneath NE China: New constraints on intraplate volcanism, deep
602 subduction and their potential link. *Earth and Planetary Science Letters* 412, 101-111.
603 <https://doi.org/10.1016/j.epsl.2014.12.019>.

604 Maruyama, S., Hasegawa, A., Santosh, M., Kogiso, T., Omori, S., Nakamura, H., Kawai, K., Zhao, D., 2009. The
605 dynamics of big mantle wedge, magma factory, and metamorphic-metasomatic factory in subduction zones.
606 *Gondwana Research* 16, 414-430. <https://doi.org/10.1016/j.gr.2009.07.002>.

607 Niu, F., Li, J., 2011. Component azimuths of the CEArray stations estimated from P wave particle motion. *Earthq. Sci.*
608 24, 3-13. <http://dx.doi.org/10.1007/s11589-011-0764-8>.

609 Rawlinson, N., Sambridge, M., 2004a. Multiple reflection and transmission phases in complex layered media using a
610 multistage fast marching method. *Geophysics* 69, 1338-1350. <https://doi.org/10.1190/1.1801950>.

611 Rawlinson, N., Sambridge, M., 2004b. Wave front evolution in strongly heterogeneous layered media using the fast-
612 marching method. *Geophysical Journal International* 156, 631-647. <https://doi.org/10.1111/j.1365-246X.2004.02153.x>.

613

614 Ringwood, A.E., 1962. A model for the upper mantle: 2. *J. Geophys. Res.* 67, 4473-4478.
615 <https://doi.org/10.1029/JZ067i011p04473>.

616 Sun, Y., Liu, J., Tang, Y., Chen, J., Zhou, K., Chen, B., 2016. Structure of the Upper Mantle and Transition Zone
617 Beneath the South China Block Imaged by Finite Frequency Tomography. *Acta Geologica Sinica - English*
618 Edition 90, 1637-1652. <https://doi.org/10.1111/1755-6724.12807>.

619 Tao, K., Grand, S.P., Niu, F., 2018. Seismic Structure of the Upper Mantle Beneath Eastern Asia From Full Waveform
620 Seismic Tomography. *Geochem. Geophys. Geosyst.* 19, 2732-2763. <https://doi.org/10.1029/2018GC007460>.

621 Trampert, J., Vacher, P., Vlaar, N., 2001. Sensitivities of seismic velocities to temperature, pressure and composition
622 in the lower mantle. *Physics of the Earth and Planetary Interiors* 124, 255-267. [https://doi.org/10.1016/S0031-9201\(01\)00201-1](https://doi.org/10.1016/S0031-9201(01)00201-1).

623

624 Wei, S.S., Chen, Y.J., 2016. Seismic evidence of the Hainan mantle plume by receiver function analysis in southern
625 China. *Geophys. Res. Lett.* 43, 8978-8985. <https://doi.org/10.1002/2016GL069513>.

626 Wessel, P., Smith, W. H. F., Scharroo, R., Luis, J., Wobbe, F., 2013. Generic mapping tools: improved version released.
627 *Eos, Transactions American Geophysical Union* 94, 409-410. <https://doi.org/10.1002/2013EO450001>.

628 Xia, S., Zhao, D., Sun, J., Huang, H., 2016. Teleseismic imaging of the mantle beneath southernmost China: New
629 insights into the Hainan plume. *Gondwana Research* 36, 46-56. <https://doi.org/10.1016/j.gr.2016.05.003>.

630 Xu, M., Huang, H., Huang, Z., Wang, P., Wang, L., Xu, M., Mi, N., Li, H., Yu, D., Yuan, X., 2018. Insight into the
631 subducted Indian slab and origin of the Tengchong volcano in SE Tibet from receiver function analysis. *Earth and*
632 *Planetary Science Letters* 482, 567-579. <https://doi.org/10.1016/j.epsl.2017.11.048>.

633 Zhang, R., Wu, Y., Gao, Z., Fu, Y. V., Sun, L., Wu, Q., Ding, Z., 2017. Upper mantle discontinuity structure beneath
634 eastern and southeastern Tibet: new constraints on the Tengchong intraplate volcano and signatures of detached

635 lithosphere under the western Yangtze craton. *J. Geophys. Res. Solid Earth* 122, 1367-1380.
636 <https://doi.org/10.1002/2016JB013551>.

637 Zhang, Y., Niu, F., Ning, J., 2022. Mantle transition zone beneath northeast China imaged by receiver function data
638 using fast marching eikonal solver based 3-D migration. *Chinese J. Geophys.*, (in Chinese). 65, 2945-2959.
639 <https://doi.org/10.6038/cjg2022P0596>.

640 Zhao, G., 2015. Jiangnan Orogen in South China: Developing from divergent double subduction. *Gondwana Research*
641 27, 1173-1180. <https://doi.org/10.1016/j.gr.2014.09.004>.

642 Zheng, Y., Zhang, S., 2007. Formation and evolution of Precambrian continental crust in South China. *Chinese Sci.*
643 *Bull.* 52, 1-12. <https://doi.org/10.1007/s11434-007-0015-5>.

644 Zheng, X., Ouyang, B., Zhang, D., Yao, Z., Liang, J., Heng J., 2009. Technical system construction of Data Backup
645 Centre for China Seismograph Network and the data support to researches on the Wenchuan earthquake. *Chinese*
646 *J. Geophys.*, (in Chinese). 52, 1412-1417. <https://doi.org/10.3969/j.issn.0001-5733.2009.05.031>.

647 Zhou, L., Xie, J., Shen, W., Zheng, Y., Yang, Y., Shi, H., Ritzwoller, M.H., 2012. The structure of the crust and
648 uppermost mantle beneath South China from ambient noise and earthquake tomography. *Geophysical Journal*
649 *International* 189, 1565-1583. <https://doi.org/10.1111/j.1365-246X.2012.05423.x>.

650 Zhou, X.M., Li, W.X., 2000. Origin of Late Mesozoic igneous rocks in Southeastern China: implications for
651 lithosphere subduction and underplating of mafic magmas. *Tectonophysics* 326, 269-287.
652 [https://doi.org/10.1016/S0040-1951\(00\)00120-7](https://doi.org/10.1016/S0040-1951(00)00120-7).

653

654